A Fast-Transient Boost Converter With Peak Passive Ripple Mode Control and AC Couple

Yi-Rong Huang, Ching-Jan Chen, *Senior Member, IEEE*, Jia-Cheng Wu, and Tsung-Wei Huang

***Abstract*—Peak current mode (PCM) control is often used nowadays in boost converters to improve the stability and control bandwidth because of its single pole characteristic. However, the slope of inductor current causes large output voltage deviation and settling time during load-transient. This article proposes a peak passive ripple mode (PPRM) control with ac couple to solve the aforementioned load-transient issue. PPRM control generates a passive ripple for modulation and couples output voltage signal by the passive RC circuit to achieve a fast transient response. Thus, the current sensor and active circuits can be eliminated. Small signal models are proposed for proposed controls. The experiment and simulation results verified the superior load-transient response of the proposed control with the best figure-of-merit among the recent papers. Compare PPRM control with ac couple to PCM control, the output voltage undershoot/overshoot during load step-up/down reduces to only 42% and 38%, respectively. The proposed small signal models also match the experimental results.**

***Index Terms*—DC-DC power converters, modeling, pulse width modulation converters.**

I. Introduction

THE boost converter is widely used to output a higher-than-input voltage to a load with the transient requirement. Recently, boost converters found applications in portable devices applications such as power management integrated circuits and USB On-The-Go (OTG) [1], [2]. OTG is a specification that allows portable devices, such as tablets or smartphones, to provide power to another USB peripheral device, such as a mouse, keyboard, USB disk, etc. Fig. 1 shows the OTG system structure for portable devices. Li-ion batteries are usually used in portable devices, and the USB bus specification is 5 V. Thus, a boost converter is required to handle the power delivery. In an OTG application, the load-transient performance is one of the significant specifications for a boost converter. As shown in Fig. 2, the output current of boost converter changes during USB peripheral devices plugging where the maximum current of USB 3.0 is up to 1.5 A.

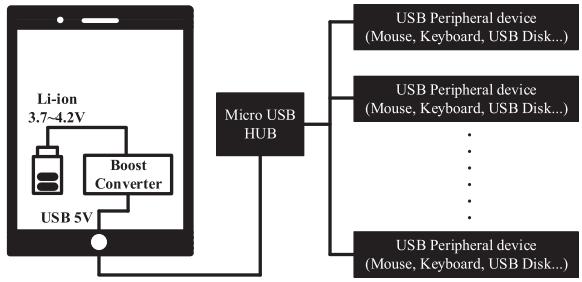

Fig. 1. System structure of OTG application for portable devices.

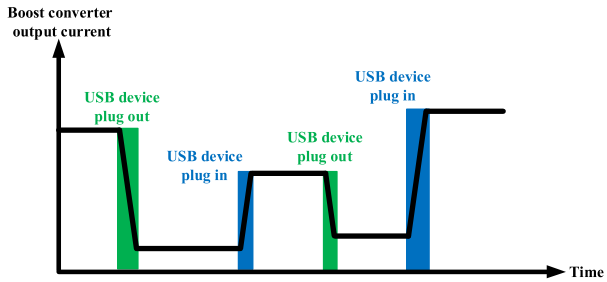

Fig. 2. Boost output current on OTG application.

Peak current mode (PCM) control has been widely used in boost converters nowadays, as shown in Fig. 3 [3], [4]. The boost converter has right-half-plane (RHP) zero, which causes phase angle dropping. Since PCM turns the LC complex poles of the power stage into a single pole on V_c to V_{out} transfer function. Designing the compensator to achieve loop stability and larger bandwidth is easier.

However, PCM control has a drawback that diminishes load-transient performance. As shown in (1), the inductor current falling slope, $S_{f,il}$, of boost converter has output voltage V_{out} information. Equation (2) is obtained by perturbating V_{out}. It shows that the variation of falling slope is in negative proportion to the variety of V_{out}, which causes slower load-transient performance. As shown in Fig. 4, after a load increase, V_{out} drops, which reduces the absolute value of $S_{f,il}$. Thus, the inductor current ramp is closer to V_c, and the on-time at the next cycle, $T_{on(2)}$, reduces. The small on-time causes a larger output voltage undershoot.

$$S_{f,il} = \frac{di_L}{dt} = \frac{1}{L}\left(V_{in} - V_{out}\right) \tag{1}$$

Manuscript received 17 April 2023; revised 20 June 2023; accepted 20 July 2023. Date of publication 1 August 2023; date of current version 1 September 2023. This work was supported in part by Richtek Technology Corporation, Taiwan, and in part by the National Science and Technology Council, Taiwan. Recommended for publication by Associate Editor M. Ponce-Silva. *(Corresponding author: Ching-Jan Chen.)*

Yi-Rong Huang, Ching-Jan Chen, and Jia-Cheng Wu are with the Department of Electrical Engineering, National Taiwan University, Taipei 10617, Taiwan (e-mail: ggcadog@gmail.com; chenjim@ntu.edu.tw; smilejack-129676@gmail.com).

Tsung-Wei Huang is with the Richtek Technology Corporation, Hsinchu 30288, Taiwan (e-mail: willie_huang@richtek.com).

Color versions of one or more figures in this article are available at https://doi.org/10.1109/TPEL.2023.3300465.

Digital Object Identifier 10.1109/TPEL.2023.3300465

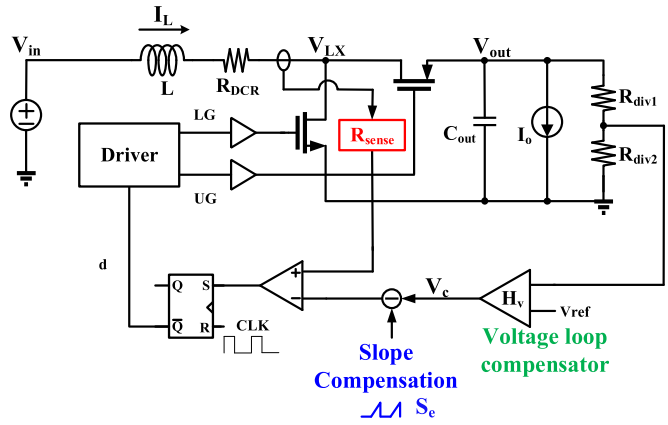

Fig. 3. Boost converter with PCM control.

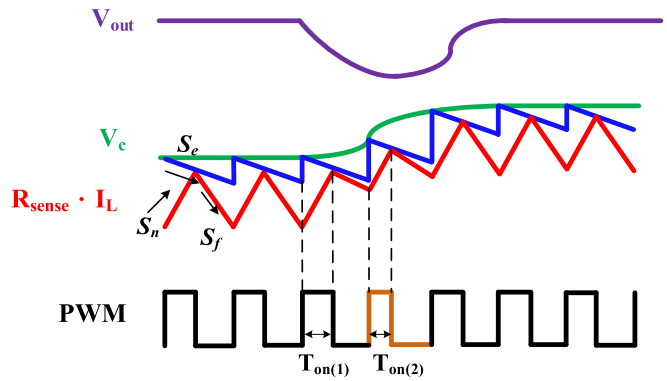

Fig. 4. Load-transient behavior of boost converter with PCM control.

$$S_{f,il} + \hat{S}_{f,il} = \frac{di_L}{dt} + \frac{d\hat{i}_L}{dt} = \frac{1}{L}(V_{in} - V_{out}) - \frac{1}{L}\hat{v}_{out}. \quad (2)$$

Several techniques are proposed to improve the transient performance of current mode control. First, fast-response current sensors are proposed to increase the speed of the current loop [5], [6], [7]. Furthermore, pulse frequency modulation (PFM) is also widely used to improve the transient performance of current mode control because the PFM has variable switching frequency during transient [5], [6], [7], [8], [9], [10], [11], [12], [13]. However, the load transient performances of these controls are still limited by the increased falling slope of sensed inductor current during load increase as shown in Fig. 4. This is because the inductor current signal is used as a modulation signal.

The ripple-based control method has been used to improve transient performance [14], [15], [16], [17], [18], [19], [20]. The ripple-based control uses v_{out} ripple as a modulation ramp, which directly forms a fast response loop to achieve good transient performance. However, the fast response loop of ripple-based control has subharmonic stability issue when the low equivalent series resistance (ESR) output capacitors, such as ceramic capacitors, are used [17], [21], [22], [23]. To solve the stability issue, the compensation ramp is added with v_{out} ripple [9], [16], [24], [25]. However, mixing the compensation ramp with v_{out} ripple requires an additional adder. Besides, the added compensation ramp often makes the transient response slower. Alevoor et al. [26] propose a peak current fast feedback control (PFFC). The PFFC adds a fast v_{out} feedback path with an inductor current signal to improve load-transient performance. The concept of PFFC is like ripple-based control. However, the inductor current signal diminishes the transient performance as shown in Fig. 4.

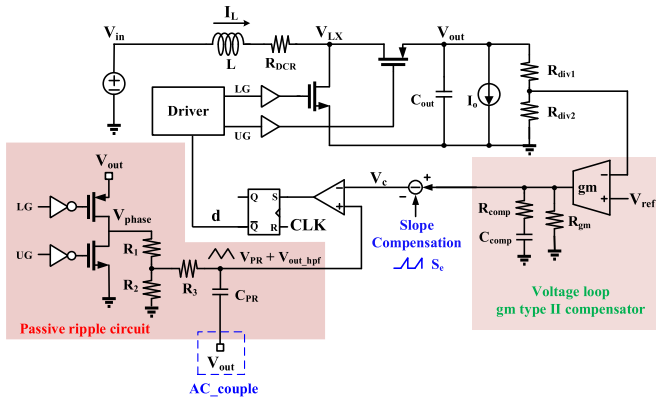

Fig. 5. Boost converter with PPRM control and ac couple.

This article proposes a peak passive ripple mode (PPRM) control with ac couple, as shown in Fig. 5, for a boost converter to improve the aforementioned load transient response issue. PPRM control generates a passive ripple (PR) for modulation by a passive RC circuit. Thus, the current sensor, active circuits, and their related power consumption can be eliminated. The variation of PR rising slope $S_{n,PR}$ is in positive proportion to the variety of $V_{out.}$ Thus, unlike current mode control, the on-time is extended by $S_{n,PR}$ during V_{out} dropping to get better transient performance. The ac couple mixes the PR with V_{out} by passive RC circuit, so an additional adder is not required. During V_{out} transient, the ac couple path quickly extends or contracts the on-time to get good transient performance. With the feature of fast transient response and current sensor elimination, the proposed control is suitable for mobile device applications such as cellphones, notebooks, and cars. Small signal models for a boost converter with PPRM control and ac couple are proposed in this article. Control to output transfer function $G_{vc}(s)$ with the pole-zero form is derived to facilitate the controller design.

This article is organized as follows. The circuit description and behavior of PPRM control without ac couple are presented in Section II. The proposed small signal model for PPRM control without ac couple is presented in Section III. Both circuit behavior and small signal model of PPRM control with ac couple are presented in Section IV. Experiment verifications and load-transient comparisons are demonstrated in Section V.

II. Boost Converter With PPRM Control

A. PR Circuit Description

The boost converter with PPRM control is shown in Fig. 6. The difference between Figs. 5 and 6 is that ac_couple point in Fig. 6 is connected to the ground. The PR circuit composes of a PMOS, NMOS, and an RC low pass filter. R_1 and R_2 form a voltage divider to adjust PR amplitude. The PMOS of the PR

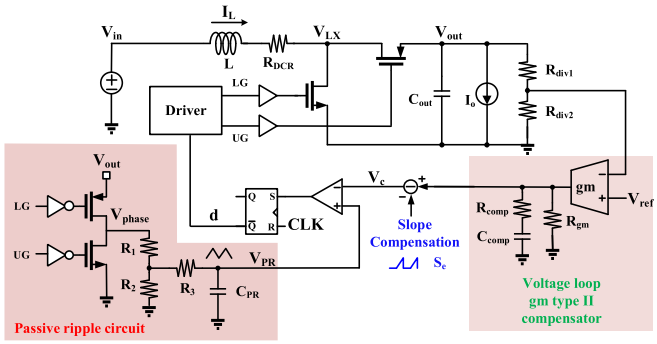

Fig. 6. Boost converter with PPRM control.

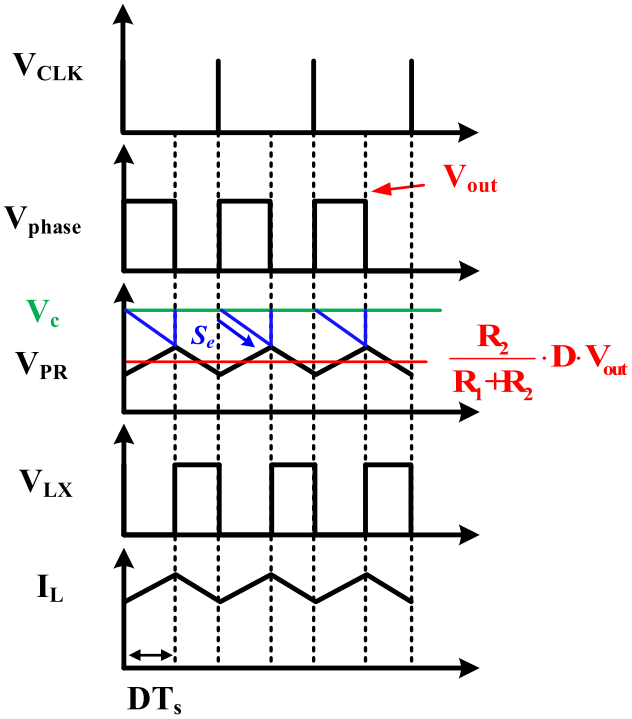

Fig. 7. Steady-state waveform of boost converter with PPRM control.

circuit turns ON during the low-side MOS in the power stage turning ON, and the NMOS of the PR circuit turns ON during the high-side MOS in the power stage turning ON. The PR is obtained by charging capacitor C_{PR} when V_{phase} is tied to V_{out} and discharging C_{PR} when V_{phase} is tied to the ground. If the RC time constant is much larger than the switching period, the slope of PR is approximated as a constant value during charging or discharging. The key waveforms are shown in Fig. 7. It can be seen that PR is in phase with inductor current. As will be analyzed, PR has slopes proportional to the inductor current ripple at steady-state. Besides, the variety of PR rising slope $S_{n,PR}$ is in positive proportion to the variety of V_{out}. Unlike the inductor current signal, the PR signal would extend the on-time during V_{out} undershoot and gets a better transient response.

B. Rising Slope Analysis of PR

The PR rising slope $S_{n,PR}$ can be derived by the below procedure. PR rising slope $S_{n,PR}$ is obtained as (3) from differential

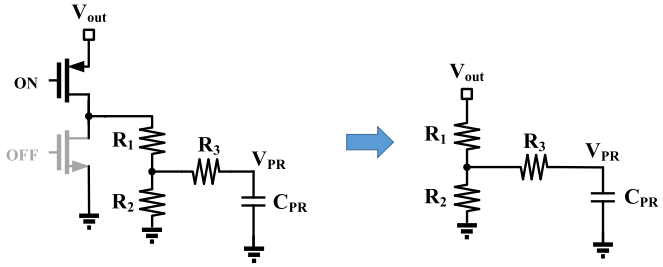

Fig. 8. Equivalent circuit of PR circuit during on-time.

equation describing the equivalent circuit of PR circuit during on-time in Fig. 8. Generally, the ripple of V_{PR} is much smaller than the dc value of V_{PR}. Therefore, the $v_{PR}(t)$ in (3) can be approximated to the dc value of V_{PR}. The dc value of V_{PR} is the average value of V_{phase} divided by R_1 and R_2 network as shown in Fig. 7. Since the dc value of V_{PR} is $D{\cdot}V_{out} \cdot R_2/(R_1 + R_2)$, (4) can be obtained by substituting the dc value of V_{PR} into (3). Equation (4) can be represented as (5). By substituting the transfer duty ratio of the boost converter into (5), (6) can be obtained. In (6), it can be found that the PR rising slope $S_{n,PR}$ at steady-state is in proportion to V_{in}, which is in proportion to the inductor current rising slope of the boost converter.

$$S_{n,PR} = \frac{dv_{PR}(t)}{dt} = \frac{1}{R_{EQ}C_{PR}}\frac{R_2}{R_1+R_2} \cdot V_{out} - \frac{1}{R_{EQ}C_{PR}}v_{PR}(t) \tag{3}$$

Where

$$R_{EQ} = \frac{R_1R_2 + R_1R_3 + R_2R_3}{R_1+R_2}$$

$$S_{n,PR} = \frac{1}{R_{EQ}C_{PR}}\frac{R_2}{R_1+R_2} \cdot V_{out} - \frac{1}{R_{EQ}C_{PR}}\frac{R_2}{R_1+R_2} \cdot D \cdot V_{out} \tag{4}$$

$$S_{n,PR} = \frac{1}{R_{EQ}C_{PR}}\frac{R_2}{R_1+R_2} \cdot (1-D) \cdot V_{out} \tag{5}$$

$$S_{n,PR} = \frac{1}{R_{EQ}C_{PR}}\frac{R_2}{R_1+R_2} \cdot V_{in} \tag{6}$$

The ac response of PR rising slope can be derived by the below procedure. By perturbing V_{out} in (3) and assuming $v_{PR}(t)$ approximate to dc value of V_{PR}, (7) can be derived. (8) can be obtained by rearranging (7).

$$S_{n,PR} + \hat{S}_{n,PR} = \frac{1}{R_{EQ}C_{PR}}\frac{R_2}{R_1+R_2} \cdot (V_{out} + \hat{v}_{out}) - \frac{1}{R_{EQ}C_{PR}} \cdot DV_{out} \tag{7}$$

$$S_{n,PR} + \hat{S}_{n,PR} = \frac{1}{R_{EQ}C_{PR}}\frac{R_2}{R_1+R_2} \cdot V_{in} + \frac{1}{R_{EQ}C_{PR}}\frac{R_2}{R_1+R_2} \cdot \hat{v}_{out}. \tag{8}$$

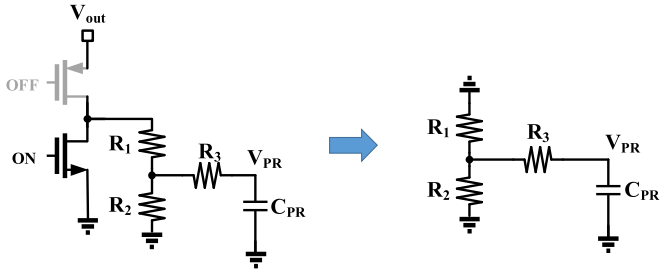

Fig. 9. Equivalent circuit of PR circuit during OFF-time.

From (8), it can be found that the changing of PR rising slope $S_{n,PR}$ is in positive proportion to the changing of V_{out}. Therefore, PPRM control extends more on-time than PCM control during v_{out} voltage dropping and gets better load-transient performance.

C. Falling Slope Analysis of PR

The PR falling slope $S_{f,PR}$ can be derived by the same procedure for rising slope analysis. PR falling slope $S_{f,PR}$ is obtained as (9) from the differential equation describing the equivalent circuit of PR circuit during OFF-time in Fig. 9. Assuming the $v_{PR}(t)$ in (9) can be approximated to dc value of V_{PR}, (10) can be obtained. By substituting the transfer duty ratio of the boost converter into (10), (11) can be obtained. In (11), it can be found that the PR falling slope $S_{f,PR}$ is in proportion to V_{in}-V_{out}, which is in proportion to inductor current rising slope of the boost converter. The ac response of PR falling slope can be derived by perturbing V_{out} in (9) and assuming $v_{PR}(t)$ approximate to dc value of V_{PR}. Thus, unlike inductor current ripple, $S_{f,PR}$ does not vary with V_{out}.

$$S_{f,PR} = \frac{dv_{PR}(t)}{dt} = \frac{-1}{R_{EQ}C_{PR}} v_{PR}(t) \tag{9}$$

$$S_{f,PR} = \frac{-1}{R_{EQ}C_{PR}} \cdot \frac{R_2}{R_1 + R_2} \cdot D \cdot V_{out} \tag{10}$$

$$S_{f,PR} = \frac{-1}{R_{EQ}C_{PR}} \cdot \frac{R_2}{R_1 + R_2} \cdot (V_{in} - V_{out}). \tag{11}$$

D. Power Consumption Analysis of PR Circuit

The power consumption of the PR circuit can be calculated by multiplying the current I_{con} flowing out of V_{out} source when the PMOS turns ON. To calculate consumption current I_{con}, we assume the V_{PR} is a constant voltage source with the dc value of V_{PR} as shown in Fig. 10 because the ripple of V_{PR} is apparently smaller than the dc value of V_{PR}. By the equivalent circuit shown in Fig. 10, the consumption current I_{con} can be derived as (12). Observing (12) shows that the maximum consumption current is as (13). Therefore, the maximum power consumption of PR circuit can be obtained by multiplying (13) with V_{out} as (14). If the controller is implemented in an integrated circuit (IC), the resistance of R_1, R_2, and R_3 can be MΩ grade. Taking example conditions that R_1, R_2, and R_3 are equal to 1.2 MΩ and the V_{out}

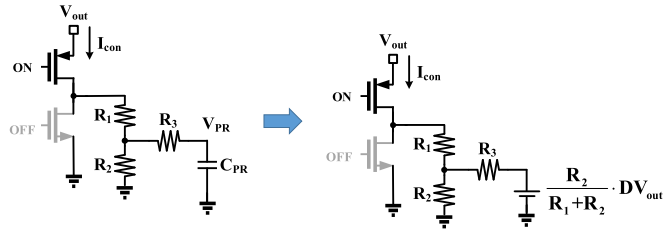

Fig. 10. Equivalent PR circuit for calculating consumption current.

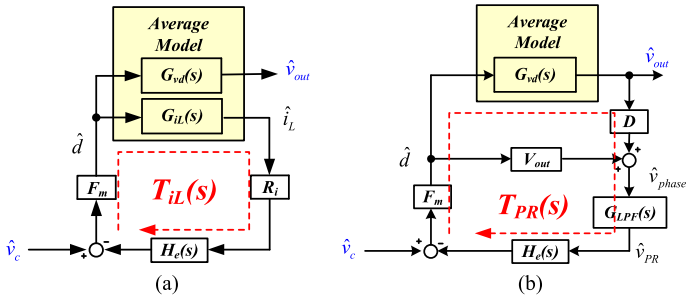

Fig. 11. Control block diagrams of PCM and PPRM controls. (a) PCM control. (b) PPRM control.

voltage is 5 V for the USB bus voltage of the OTG application, the maximum power consumption of the PR circuit is about 13.8 μW.

$$I_{con} = \frac{R_2 + R_3}{R_1R_2 + R_1R_3 + R_2R_3} \cdot V_{out} - \frac{\frac{R_2^2}{R_1+R_2}}{(R_1R_2 + R_1R_3 + R_2R_3)} \cdot DV_{out} \tag{12}$$

$$I_{con\_max} = \frac{R_2 + R_3}{R_1R_2 + R_1R_3 + R_2R_3} \cdot V_{out} \tag{13}$$

$$P_{con\_max} = \frac{R_2 + R_3}{R_1R_2 + R_1R_3 + R_2R_3} \cdot V_{out}^2. \tag{14}$$

III. Proposed Small-Signal Model for a Boost Converter With PPRM Control

A. Small-Signal Model Derivation for PPRM Control

A small signal model for PPRM control operated in continuous conduction mode (CCM) is derived based on the modifications of Ridley's current-mode control model [27]. The difference between PCM and PPRM control is that PCM uses an inductor current signal for modulation, but PPRM uses a PR signal. Therefore, the deriving strategy is replacing Ridley's model's current loop $T_{iL}(s)$ with PR loop $T_{PR}(s)$, as shown in Fig. 11.

In Fig. 11(b), the d to v_{out} transfer function $G_{vd}(s)$ is obtained by average modeling as in [27], [28], and [29]. The v_c to d transfer function, F_m, can be derived as (15) by perturbating v_c to obtain variation in duty [27]. The sampling gain, $H_e(s)$ is expressed as (16), which is the same as PCM [27]. This is

because the waveform geometric of PCM and PPRM are the same. There are three underived control blocks in Fig. 11(b): d to v_{phase}, v_{out} to v_{phase}, and v_{phase} to v_{PR}.

$$F_m \equiv \frac{\hat{d}}{\hat{v}_c} = \frac{1}{(S_{n,PR} + S_e)T_s} \tag{15}$$

$$H_e(s) = \frac{sT_s}{e^{sT_s} - 1}. \tag{16}$$

In this part, we start to derive d to v_{phase}, v_{out} to v_{phase}, and v_{phase} to v_{PR} transfer functions in Fig. 11(b). By observing v_{phase} waveform in Fig. 7, we know that v_{phase} is a square wave with v_{out} amplitude and duty-cycle of D. By averaging v_{phase}, (17) can be obtained. By perturbating (17), (18) can be obtained.

$$\langle v_{phase} \rangle_{ave} = D \cdot v_{out} \tag{17}$$

$$\hat{v}_{phase} = v_{out} \cdot \hat{d} + D \cdot \hat{v}_{out}. \tag{18}$$

Equation (18) shows that d to v_{phase} and v_{out} to v_{phase} transfer function is a simple constant value of v_{out} and D, respectively. The v_{phase} to v_{PR} transfer function is a low-pass RC filter gain, as can be derived in Fig. 6. By Laplace transform, the transfer function of v_{phase} to v_{PR} can be obtained as follows:

$$G_{LPF}(s) \equiv \frac{\hat{v}_{PR}}{\hat{v}_{phase}} = \frac{1}{R_{EQ}C_{PR}s + 1} \cdot \frac{R_1}{R_1 + R_2}. \tag{19}$$

In (18) and (19), the control block diagram of PPRM control can be built as shown in Fig. 11(b). The control to output transfer function $G_{vc}(s)$, defined as v_{out}/v_c, can be derived as follows:

$$G_{vc}(s) \equiv \frac{\hat{v}_{out}}{\hat{v}_c} = \frac{F_m \cdot G_{vd}(s)}{1 + F_m \cdot (V_{out} + D \cdot G_{vd}(s)) \cdot G_{LPF}(s) \cdot H_e(s)} \tag{20}$$

Where

$$G_{vd}(s) = K_{vd} \cdot \frac{\left(1 - \frac{s}{\omega_{RHP}}\right)}{\left(1 + \frac{s}{Q_{o\_vd} \cdot \omega_{o\_vd}} + \frac{s^2}{\omega_{o\_vd}^2}\right)}.$$

The parameters are summarized in Table I.

The $H_e(s)$ is an exponential function that has an infinite pole and zero, so the exponential form is not useful for the design and analysis. In order to have finite poles and zeros of $G_{vc}(s)$, we take the approximation on $H_e(s)$ [27], and (21) can be obtained.

$$H_e(s) \approx 1 + \frac{s}{\omega_n Q_z} + \frac{s^2}{\omega_n^2} \tag{21}$$

where $Q_z = \frac{-2}{\pi}, \omega_n = \frac{\pi}{T_s}$.

Substituting (21) into (20) and solving poles and zeros in the transfer function, the pole-zero form of $G_{vc}(s)$ can be obtained as $G_{vc,simp}(s)$ in (22). The parameters are summarized in Table I.

$$G_{vc\_simp}(s) = \frac{v_o(s)}{v_c(s)} \approx \frac{K_{vc} \cdot \left(1 + \frac{s}{\omega_{PR}}\right) \cdot \left(1 - \frac{s}{\omega_{RHP}}\right)}{\left(1 + \frac{s}{Q_{o\_vc} \cdot \omega_{o\_vc}} + \frac{s^2}{\omega_{o\_vc}^2}\right)\left(1 + \frac{s}{Q_n \cdot \omega_n} + \frac{s^2}{\omega_n^2}\right)}. \tag{22}$$

TABLE I
TRANSFER FUNCTION PARAMETERS OF $G_{VC}(S)$ AND $G_{VC\_SIMP}(S)$

Item	Parameters
K_{vd}	$\frac{\left((1-D)\cdot V_{out} - R_{DCR}\cdot\frac{I_o}{1-D} - R_{DCR}\cdot\frac{I_o}{1-D}\right)}{(1-D)^2}$
K_{vc}	$\frac{F_m \cdot K_{vd}}{1+\frac{R_1}{R_1+R_2}F_m\cdot(V_{out}+D\cdot K_{vd})}$
ω_{RHP}	$\frac{(1-D)^2\cdot V_{out}}{L\cdot I_o} - \frac{R_{LG}}{L} - \frac{R_{DCR}}{L}$
ω_{o_vd}	$\frac{(1-D)}{\sqrt{L\cdot C_{out}}}$
Q_{o_vd}	$\frac{(1-D)}{(1-D)^2\cdot R_{ESR} + R_{DCR} + (1-D)\cdot R_{UG} + D\cdot R_{LG}} \cdot \frac{\sqrt{L}}{\sqrt{C_{out}}}$
ω_{PR}	$\frac{1}{R_{EQ}C_{PR}}$
Q_{o_vc}	$\frac{1}{\frac{1}{Q_o}\cdot\sqrt{\frac{V_{out}}{V_{out}+D\cdot K_{vd}}} - \frac{\omega_{o\_vd}}{\omega_{RHP}}\cdot\frac{D\cdot K_{vd}}{\sqrt{V_{out}\cdot(V_{out}+D\cdot K_{vd})}} - \frac{\omega_{o\_vd}}{\omega_s}\cdot 2\pi\cdot(1-D)\cdot\left(1+\frac{S_e}{S_n}\right)\frac{D\cdot K_{vd}}{\sqrt{V_{out}\cdot(V_{out}+D\cdot K_{vd})}}}$
ω_{o_vc}	$\omega_{o\_vd}\cdot\sqrt{\frac{V_{out}+D\cdot K_{vd}}{V_{out}}}$
Q_n	$\frac{1}{\pi}\cdot\frac{1}{(1-D)\cdot(1+\frac{S_e}{S_{n,PR}}) - \frac{1}{2}}$
ω_n	$2\pi\cdot\frac{f_s}{2}$

TABLE II
CIRCUIT PARAMETERS OF THE SIMULATION

Item	Value	
Input voltage V_{in}	3.3 V	4.2 V
Output voltage V_{out}	5 V	
Output current I_o	1 A	
Switching frequency f_s	200 kHz	
Inductor L	8.8 μH	
Inductor dc resistor R_{DCR}	114 mΩ	
Output capacitor C_{out}	40 μF	
Low side power MOS turn-ON resistance R_{LG}	20 mΩ	
High side power MOS turn-ON resistance R_{UG}	20 mΩ	
PR circuit resistor R_1	560 Ω	
PR circuit resistor R_2	560 Ω	
PR circuit resistor R_3	820 Ω	
PR circuit capacitor C_{PR}	18 nF	

B. Model Verifications by Simulation

Equations (20) and (22) are verified by the SIMPLIS simulation tool. In previous researches, the SIMPLIS behavior circuit has proved its accuracy in predicting small-signal and dynamic response behavior [16], [30], [31], [32], [33], [34]. The model

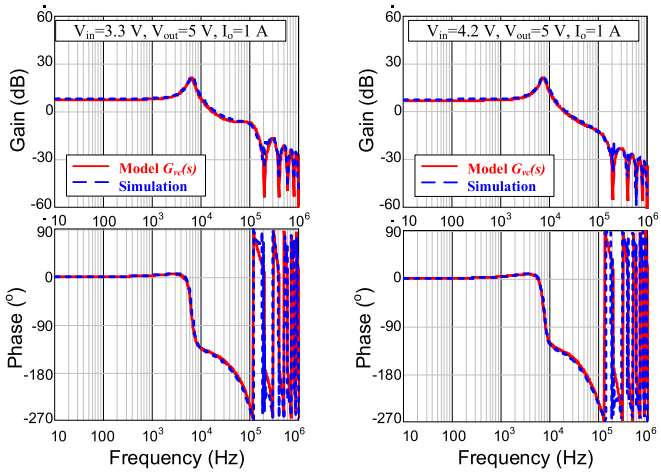

Fig. 12. $G_{vc}(s)$ verification by simulation.

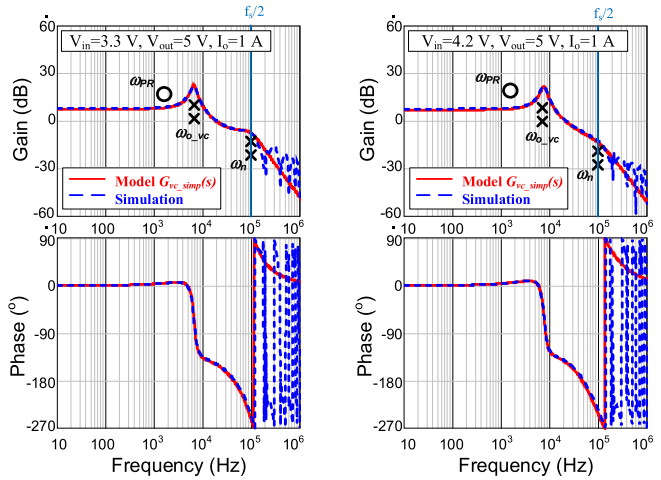

Fig. 13. $G_{vc\_simp}(s)$ verification by simulation.

of power MOSFET is a voltage-controlled switch with finite on-resistance, which shows a similar load transient response with the power MOSFET model provided by the manufacturer. The gm compensator is composed of voltage control current source, the output resistor of operational transconductance amplifier and compensation impedance. The other logic components use the built-in library in SIMPLIS. The circuit parameters and working conditions are shown in Table II. In order to cover the voltage range of Li-battery, the working condition includes V_{in} 3.3 V and 4.2 V.

Equation (20) well matches the simulation even beyond switching frequency as shown in Fig. 12. Equation (22) matches simulation up to half-switching frequency as shown in Fig. 13.

C. Comparison of Control to Output Transfer Function Between PPRM and PCM Control

In this part, we would like to compare poles and zeros of the $G_{vc}(s)$ between PPRM and PCM control. As shown in Fig. 13, the PPRM has a complex pole at half-switching frequency ω_n,

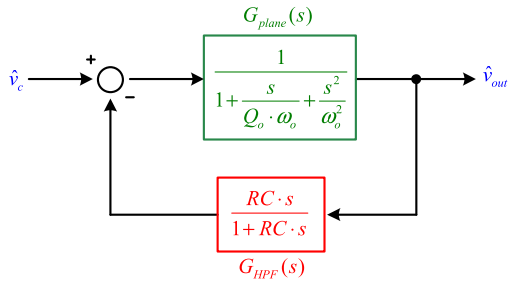

Fig. 14. Control block diagram for reducing Q factor of LC complex pole.

which is the same as PCM by referencing (22) and [27]. This means that the PPRM also has subharmonic oscillation like PCM and the stability criterion is the same as PCM. The main difference is that PPRM has an LC complex pole ω_{o_vc}, but PCM has a single pole. Besides, PPRM has an additional zero ω_{PR} named PR zero. The PR zero can be used to boost unwanted phase angle drop due to LC complex pole ω_{o_vc}, but the PR zero cannot turn the LC complex pole ω_{o_vc} to a single pole. There is a method called ac couple that can reduce Q_{o_vc} so that the peaking of LC complex pole ω_{o_vc} can be reduced and the phase angle dropping can be smoothed. We will discuss it in the next section.

IV. Improve Boost Converter With PPRM Control by AC Couple

Adding ac couple into PPRM control is proposed in this section to reduce the Q_{o_vc} of the simplified G_{vc} transfer function for easier loop compensation. In order to explain why ac couple can reduce the Q_{o_vc}, a generalized concept is proposed in Section IV-A. In Section IV-B, the circuit behavior of PPRM control with ac couple for boost converter is analyzed. In Section IV-C, it is proved that the Q_{o_vc} is reduced by ac couple concept.

A. Concept for Reducing Quality Factor (Q Factor) of Complex Pole by Adding a Feedback Loop

Fig. 14 shows a complex pole system $G_{Plane}(s)$ with a feedback loop from v_{out} to v_c through a high pass filter $G_{HPF}(s)$. The v_c to v_{out} transfer function in Fig. 14 can be derived as follows:

$$G_{vc\_concept} \equiv \frac{v_o(s)}{v_c(s)} = \frac{G_{Plane}(s)}{1 + G_{HPF}(s) \cdot G_{Plane}(s)}. \quad (23)$$

Fig. 15 shows the bode plot of $G_{Plane}(s)$, $G_{HPF}(s).G_{Plane}(s)$, $1 + G_{HPF}(s).G_{Plane}(s)$, and $G_{vc\_concept}(s)$ in (24). It is worth to mentioning that the high pass filter corner frequency of $G_{HPF}(s)$ is designed the same as ω_{o_vc}. In Fig. 16, the bode plot of $G_{HPF}(s).G_{Plane}(s)$ have a peaking beyond 0 dB and the peaking comes from ω_{o_vc}, the complex pole of $G_{Plane}(s)$. From (24), the v_c to v_{out} transfer function after closing the loop is $G_{Plane}(s)$ divided by $[1 + G_{HPF}(s).G_{Plane}(s)]$. Thus, the complex pole peaking is reduced by the peaking of $[1 + G_{HPF}(s).G_{Plane}(s)]$, and the Q factor of complex pole is reduced after closing the loop as shown in Fig. 15. This concept can be extended to the system which has complex pole and can feed v_{out} back to v_c

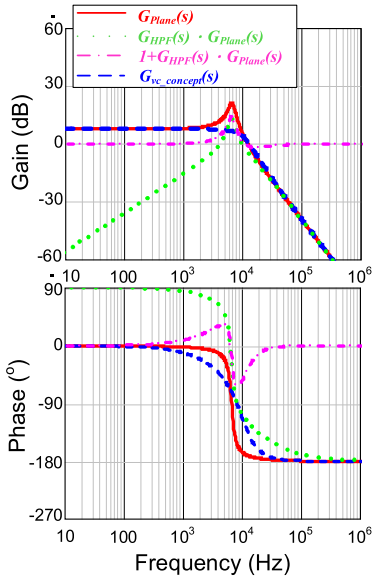

Fig. 15. Bode plot of the transfer functions in (22).

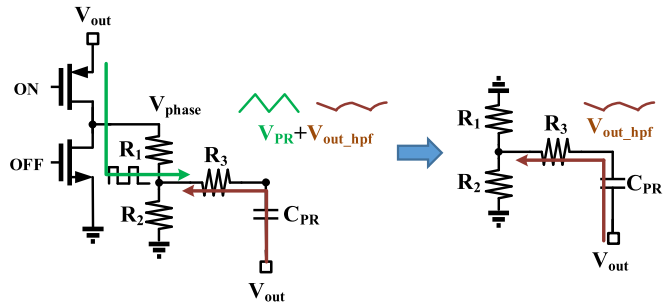

Fig. 16. Analyze ac couple behavior by superposition.

such as voltage mode control which mixes the sawtooth with v_{out} going through high pass filter.

B. Circuit Behavior of Boost Converter With PPRM Control and AC Couple

Boost convert with PPRM control and ac couple is shown in Fig. 5. The V_{out} is connected to the bottom of capacitor C_{PR}. As described in Section IV-A, the main advantage of ac couple is reducing the Q_{o_vc}. The ac couple behavior can be analyzed by superposition as shown in Fig. 16. The PR V_{PR} is mixed with V_{out_hpf}, which comes from V_{out} going through a high pass filter. The ripple slope of V_{PR} is summed with the ripple slope of V_{out_hpf}. The ripple of V_{out_hpf} is generated by V_{out} going through a high pass filter, and generally, the RC corner frequency is lower than the switching frequency. Therefore, the ripple of V_{out_hpf} is the same as the ripple of V_{out}. In Fig. 17, it can be seen that the V_{out} ripple is decided by the output capacitor current I_{Cout}, and the slope of V_{out} ripple can be derived by $dv_{out}/dt = I_{Cout}/C_{out}$. The rising and falling slope of V_{out} ripple ($S_{n,vout}$ and $S_{f,vout}$) is derived as (24) and (25). Finally, the rising and falling slope of V_{PR} mixed with V_{out_hpf} is derived by summing

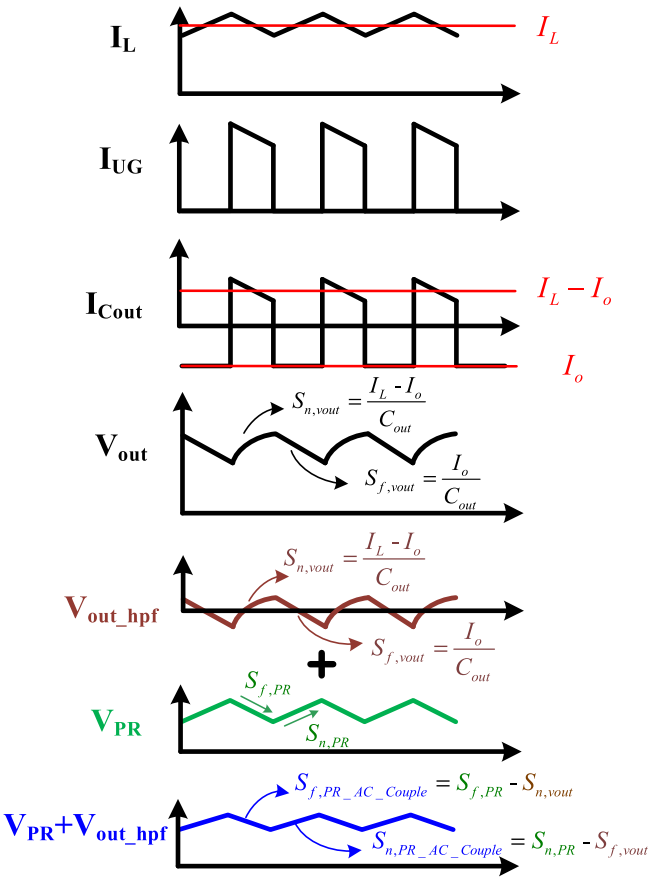

Fig. 17. Behavior waveform of PPRM with ac couple.

the slope of V_{PR} and V_{out_hpf} as (26) and (27).

$$S_{n,vout} = \frac{I_o}{C_{out}} \tag{24}$$

$$S_{f,vout} = \frac{I_L - I_o}{C_{out}} \tag{25}$$

$$S_{n,PR\_AC\_Couple} = S_{n,PR} - S_{f,vout} \tag{26}$$

$$S_{f,PR\_AC\_Couple} = S_{f,PR} - S_{n,vout}. \tag{27}$$

C. Small-Signal Model Derivation for PPRM Control With AC Couple

The control block diagram of PPRM control with ac couple can be built by adding the ac couple path into the control block diagram of PPRM control as shown in Fig. 18. In Fig. 18, the ac couple path is added by summing v_{PR} with v_{out_hpf}, which is v_{out} going through a high pass filter transfer function $G_{HPF}(s)$ shown in (28). The v_c to v_{out} transfer function for PPRM control with ac couple can be derived as (29). From (28), it can be found that the $G_{Plane\_PR\_ac}(s)$ is the v_c to v_{out} of PPRM, but the rising and falling slope parameters of $G_{Plane\_PR\_ac}(s)$ should use (26) and (27) because rising and falling slope already changed by v_{out_hpf} ripple.

$$G_{HPF}(s) = \frac{R_{EQ}C_{PR} \cdot s}{1 + R_{EQ}C_{PR} \cdot s} \tag{28}$$

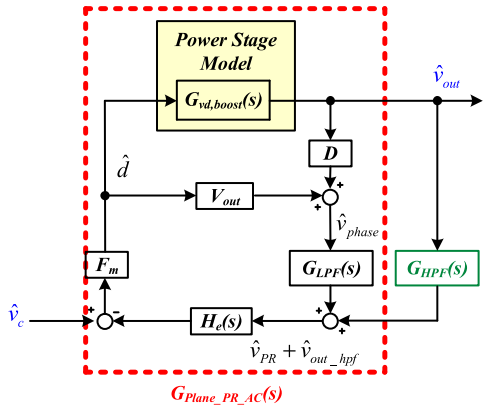

Fig. 18. Control block diagram of PPRM with ac couple.

$$G_{vc\_PR\_AC} \equiv \frac{v_o(s)}{v_c(s)} = \frac{G_{Plane\_PR\_AC}(s)}{1 + H_e(s) \cdot G_{HPF}(s) \cdot G_{Plane\_PR\_AC}(s)} \quad (29)$$

Where

$$G_{Plane\_PR\_AC}(s) = \frac{F_{m\_AC} \cdot G_{vd}(s)}{1 + F_{m\_AC} \cdot (V_{out} + D \cdot G_{vd}(s)) \cdot G_{LPF}(s) \cdot H_e(s)}$$

$$F_{m\_AC} = \frac{1}{(S_{n,PR\_AC\_Couple} + S_e)T_s}.$$

In Fig. 18, v_{out} ac couple path forms a feedback loop and reduces the Q factor of the complex pole, as mentioned in Section IV-A. The sampling gain $H_e(s)$ is a unit gain below the half-switching frequency as shown in (21). Therefore, (29) has a similar form as (23) below the half-switching frequency. In order to prove that (29) has reduced the Q factor of the complex pole, the parameters of Table II are used to draw the Bode plots of (29). Fig. 19 shows that the gain peaking and severe phase dropping of $G_{vc\_PR\_ac}(s)$ have disappeared. This means that the Q factor of the complex pole is reduced.

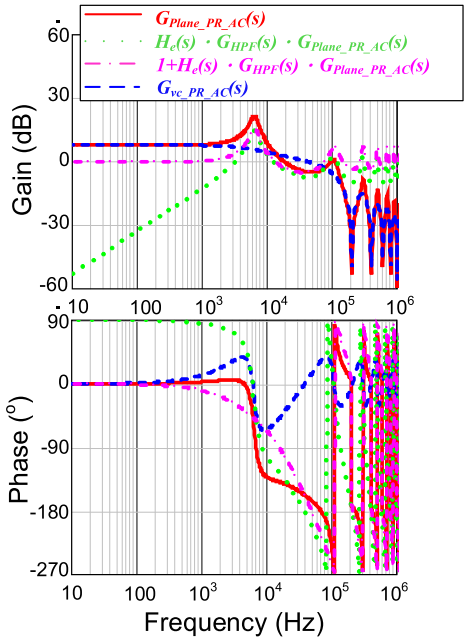

Fig. 19. Bode plot of the transfer functions in (30) for PPRM control with ac couple.

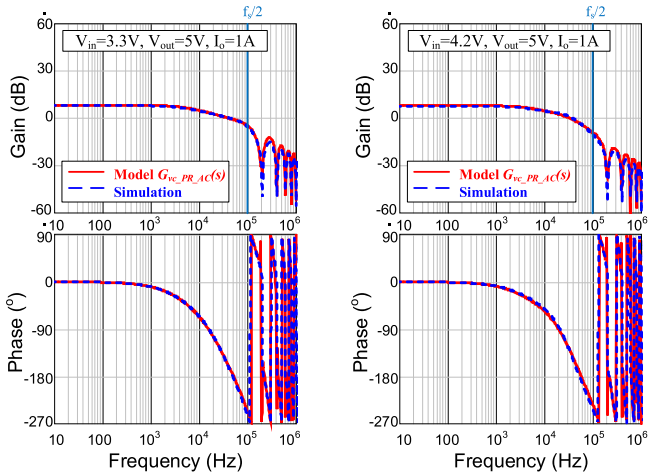

Fig. 20. $G_{vc\_PR\_ac}(s)$ verification by simulation of PPRM control with ac.

D. Model Verifications by Simulation

The control to output transfer function in (29) is verified by the SIMPLIS simulation tool. The circuit parameters and working conditions are shown in Table II. In order to cover the voltage range of the Li-battery, the working conditions include V_{in} 3.3 V and 4.2 V. The equation well match simulation results even beyond switching frequency, as shown in Fig. 20.

E. Comparison of Load-Transient Performance Between PPRM, PPRM With AC Couple, and PCM Control

In this section, a load-transient comparison of boost converter between PPRM, PPRM with ac couple, and PCM control is discussed and verified by SIMPLIS simulation. The circuit parameters and working conditions are shown in Table III. The voltage loop gains of PPRM, PPRM with ac coupe, and PCM control are defined as $T_{v\_PR}(s)$, $T_{v\_PR\_ac}(s)$ and $T_{v\_PCM}(s)$, respectively. The bandwidth of the voltage loop is one of the significant factors which affects the load-transient performance. Therefore, we compare load-transient performance based on the same voltage loop bandwidth of $T_{v\_PR}(s)$, $T_{v\_PR\_ac}(s)$ and $T_{v\_PCM}(s)$ as shown in Fig. 21.

Based on the voltage loop gain design in Fig. 21, the SIMPLIS simulated step-down and step-up load-transient results of the three controls are shown in Figs. 22 and 23, respectively. It can be seen that the PPRM with ac couple has the smallest under- and over-shoot. PPRM with ac couple also has the shortest settling time.

TABLE III
CIRCUIT PARAMETERS OF SIMULATION

Item	Value
Input voltage V_{in}	3.3 V
Output voltage V_{out}	5 V
Output current I_o	1 A
Switching frequency f_s	2.4 MHz
Inductor L	470 nH
Inductor dc resistor R_{DCR}	43 mΩ
Output capacitor C_{out}	8 μF
Low side power MOS turn-ON resistance R_{LG}	30 mΩ
High side power MOS turn-ON resistance R_{UG}	30 mΩ
PR circuit resistor R_1	1.2 MΩ
PR circuit resistor R_2	1.2 MΩ
PR circuit resistor R_3	1.2 MΩ
PR circuit capacitor C_{PR}	1.5 pF

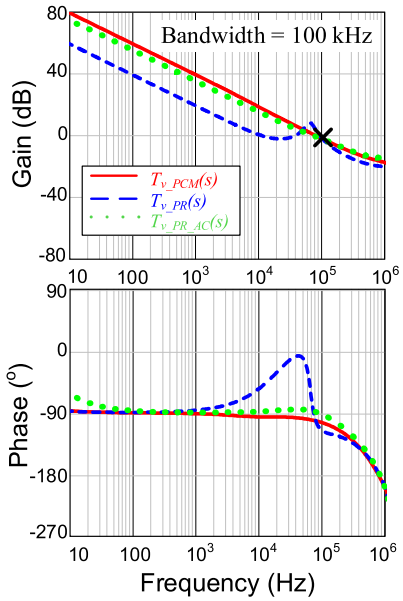

Fig. 21. Simulated voltage loop gains of $T_{v\_PR}(s)$, $T_{v\_PR\_ac}(s)$ and $T_{v\_PCM}(s)$.

V. MEASUREMENT RESULT

A boost converter with PPRM control and ac couple was implemented by discrete circuits to validate the proposed control in Fig. 5. The hardware photograph of the implemented circuit is shown in Fig. 24. The power stage is composed of two power NMOS (RQ3E100GNTB) and MOS gate driver (WCDSC006XUMA1), which has bootstrap function to drive high side NMOS. The gm compensator is composed of two operational transconductance amplifiers (OPA860ID) [35]. The adder is a V to I adding structure as shown in Fig. 25. The bandwidth of OPA860ID is up to 80 MHz, and it is enough to cover our 200 kHz switching frequency.

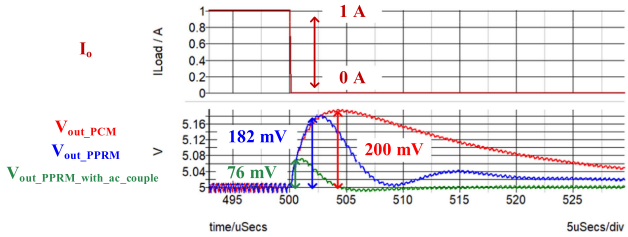

Fig. 22. Simulated step-down load-transient response (I_o from 1 to 0 A).

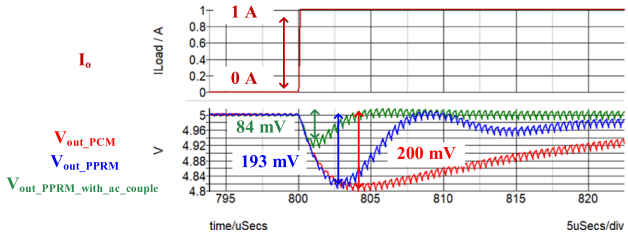

Fig. 23. Simulated step-up load-transient response (I_o from 0 to 1 A).

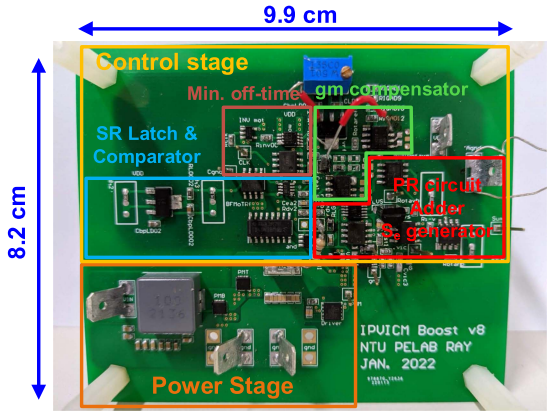

Fig. 24. Hardware photograph of boost converter with PPRM control and ac couple.

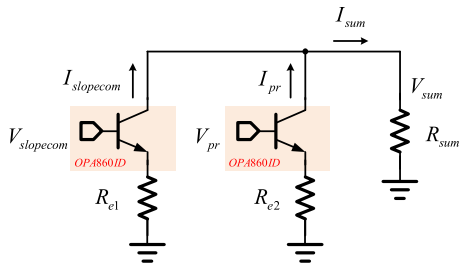

Fig. 25. V to I adder circuit.

In the implemented circuit, the slope-compensation Se is mixed with PR signal instead of V_c, but the ideal ac response is the same as the circuit mixed with V_c.

The circuit parameters and working conditions are shown in Table IV. It is worth mentioning that R_1, R_2, and R_3 are in 100 Ω range. This is because the parasitic capacitor $C_{\text{Parasitic}}$ on the printed circuit board (PCB) is in pF range at discrete component implementation. If R_1 is in MΩ range, the low-pass

TABLE IV
CIRCUIT PARAMETERS OF IMPLEMENTED CIRCUIT

Item	Value	
Input voltage V_{in}	3.3 V	4.2 V
Output voltage V_{out}	5 V	
Output current I_o	1 A	
Switching frequency f_s	200 kHz	
Inductor L	8.8 µH	
Inductor dc resistor R_{DCR}	114 mΩ	
Output capacitor C_{out}	40 µF	
Low side power MOS turn-ON resistance R_{LG}	20 mΩ	
High side power MOS turn-ON resistance R_{UG}	20 mΩ	
PR circuit resistor R_1	560 Ω	
PR circuit resistor R_2	560 Ω	
PR circuit resistor R_3	820 Ω	
PR circuit capacitor C_{PR}	18 nF	
Divider resistance R_{div1}	5 kΩ	
Divider resistance R_{div2}	5 kΩ	
Transconductance of compensator gm	1m A/V	
Output resistor of compensator R_{gm}	54 kΩ	
Compensation resistor R_{comp}	391.5 Ω	
Compensation capacitor C_{comp}	102 nF	

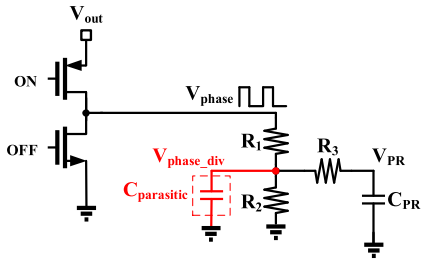

Fig. 26. PR circuit with PCB parasitic capacitor.

filter formed by $C_{\text{Parasitic}}$ and R_1 will distort the V_{PR} ramp waveform as shown in Fig. 26. Since the parasitic capacitor of PR circuit is much lower in IC implementation, R_1, R_2, and R_3 can be in MΩ range and obtain low power consumption in IC implementation.

The switching frequency is reduced to 200 kHz to mitigate the nonideal delay effects of discrete circuits. The measured steady-state waveform is shown in Fig. 27. In Fig. 27, it can be seen that the slope compensation modifies the slope of the modulation ramp, and the behavior is just like summing slope compensation with V_c.

Fig. 28 shows that the derived control to output transfer function $G_{vc\_PR\_ac}(s)$ of PPRM control with ac couple in (29) well matches with SIMPLIS simulation and measurement results up to half-switching frequency. The voltage loop gain $T_{v\_PR\_ac}(s)$ also matches with SIMPLIS simulation and measurement results, as shown in Fig. 29. The bandwidth and phase margin of voltage loop gain is 2 kHz and 97°, respectively. The measured step-down and step-up load-transient response of PPRM control

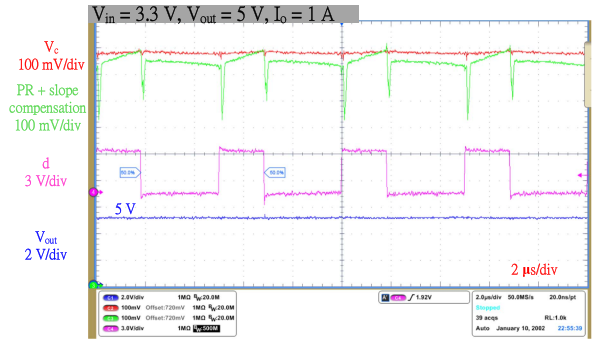

Fig. 27. Measured steady-state waveform of PPRM control with ac couple.

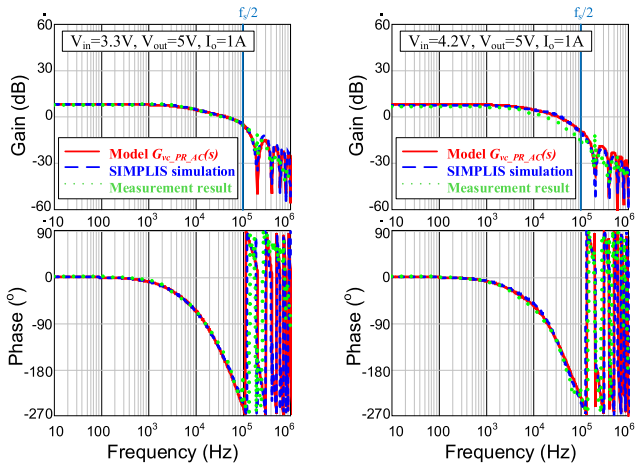

Fig. 28. Verification of $G_{vc\_PR\_ac}(s)$ by SIMPLIS simulation and measurement results.

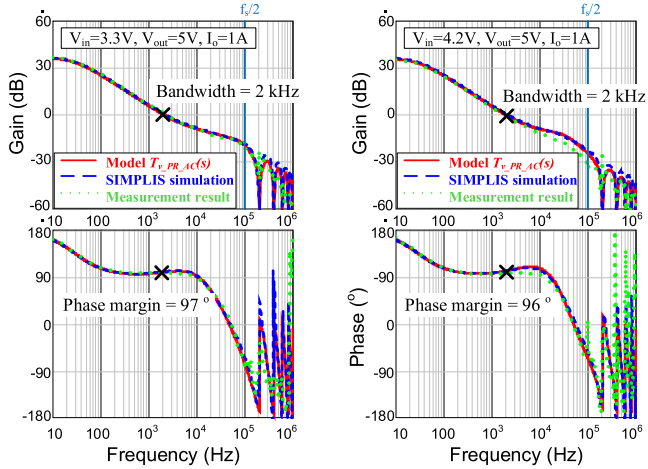

Fig. 29. Verification of $T_{v\_PR\_ac}(s)$ by SIMPLIS simulation and measurement results.

with ac couple are shown in Figs. 30 and 31, respectively, with I_o switching between 1.5 and 0.5 A.

Fig. 32 shows that the measured and simulated step-up load-transient response matches with each other for PPRM control with ac couple. The simulated load-transient behavior is close

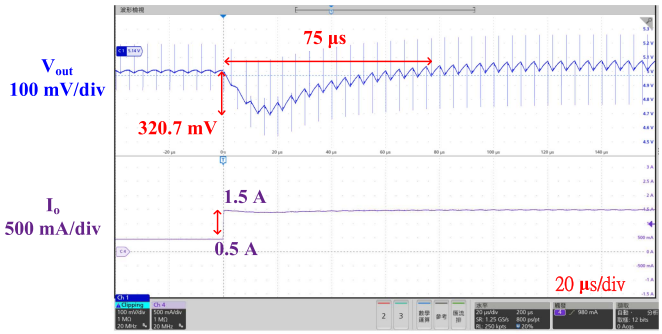

Fig. 30. Measured step-down load-transient response of PPRM control with ac couple (I_o from 1.5 to 0.5 A).

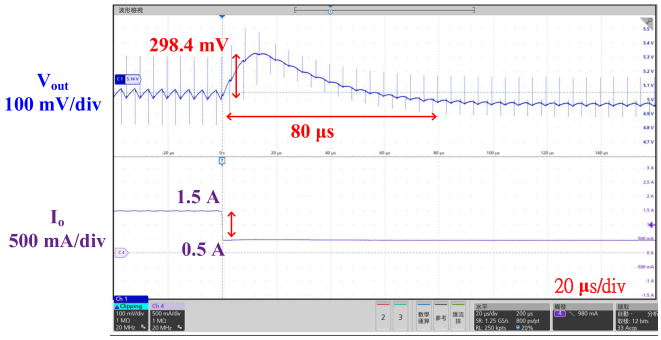

Fig. 31. Measured step-up load-transient response of PPRM control with ac couple (I_o from 0.5 to 1.5 A).

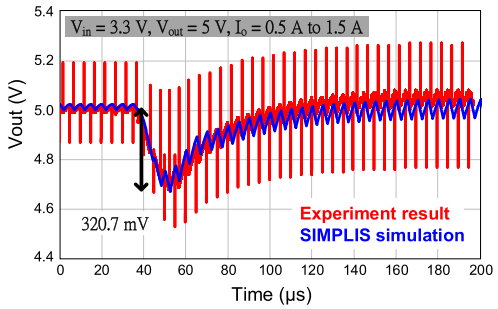

Fig. 32. Measured and simulated step-up load-transient response of PPRM control with ac couple (I_o from 0.5 to 1.5 A).

to the experiment. Therefore, the SIMPLIS simulated load-transient results of Figs. 22 and 23 can be used to predict load-transient performance.

In Figs. 22 and 23, the PPRM control with ac couple has better load-transient performance than the PCM control. The simulated output voltage overshoot during load step-down for PPRM with ac couple reduced to 38% compared with PCM control. The simulated output voltage undershoots during load step-up for PPRM with ac couple reduced to 42% compared with PCM control.

A figure of merit (FoM) is proposed to compare load-transient performance as expressed in (30). The FOM_{shoot} is composed of $v_{\rm out}$ undershoot/overshoot (Δv_{out}), load step (I_{STEP}), maximum output current ($I_{LOAD,MAX}$), output capacitance (C_{out}),

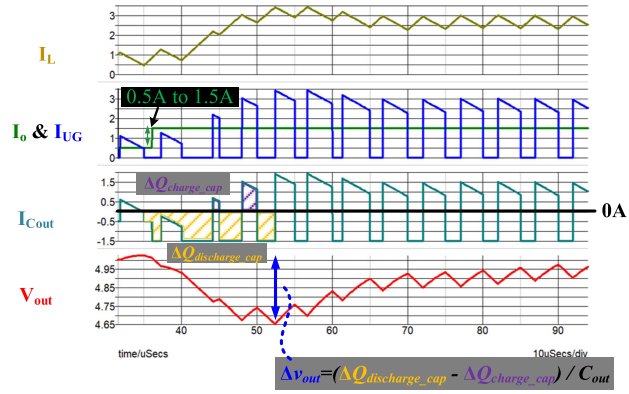

Fig. 33. Waveform of boost converter with a step load change for v_{out} undershoot analysis.

and inductance of inductor (L).

$$FOM_{shoot} = \frac{\Delta v_{out}(V) \cdot C_{out}(\mu F)}{I_{STEP}(\mathrm{A}) \cdot I_{LOAD,MAX}(A) \cdot L(\mu H)}. \quad (30)$$

The v_{out} undershoot/overshoot is a pivot to judge load-transient performance. The faster control method can achieve smaller Δv_{out}. The I_{STEP} is unquestionable since a larger load step result in a larger Δv_{out}. The $I_{LOAD,MAX}$ is a significant parameter to compare the load-transient performance of the boost converter. The larger $I_{LOAD,MAX}$ has a lower RHP zero frequency. The lower RHP zero frequency limits the voltage loop bandwidth and the load-transient performance. Therefore, the denominator of FOM_{shoot} should add $I_{LOAD,MAX}$, because larger $\mathrm{I_{LOAD,MAX}}$ has lower voltage loop bandwidth.

The consideration of output capacitance (C_{out}) and inductance (L) is explained by the waveforms of a boost converter with a step load change, as illustrated in Fig. 33. In Fig. 33, the current of the output capacitor ($\mathrm{I_{Cout}}$) is equal to upper power-MOS current ($\mathrm{I_{UG}}$) subtracted with output current ($\mathrm{I_o}$). The yellow area of $\mathrm{I_{Cout}}$ is discharged charge of the output capacitor ($\Delta Q_{discharge\_cap}$), and the purple area of $\mathrm{I_{Cout}}$ is the charged charge of the output capacitor (ΔQ_{charge_cap}). The $\mathrm{v_{out}}$ undershoot (Δv_{out}) is equal to ($\Delta Q_{discharge\_cap} - \Delta Q_{charge\_cap}$)/$C_{out}$. The above expression shows that a larger C_{out} has a smaller Δv_{out}. Therefore, the C_{out} should be added to the numerator of FOM_{shoot}. We also know that smaller ($\Delta Q_{discharge\_cap} - \Delta Q_{charge\_cap}$) can obtain smaller Δv_{out}. There are two methods to reduce ($\Delta Q_{discharge\_cap} - \Delta Q_{charge\_cap}$). The first one is to adjust the duty cycle faster using the controller. The second method is to decrease the inductance of inductor (L), which allows for a quicker increase in the inductor current, thereby reducing the discharged area $\Delta Q_{discharge\_cap}$ and increasing charged area ΔQ_{charge_cap}. Consequently, the L is one of the parameters that need to be considered. Therefore, inductance is added to the denominator of FOM_{shoot} because smaller inductance has a smaller Δv_{out}.

In Table V, the proposed control is compared with the state-of-the-art solutions proposed to improve transient performance. The references include ripple-based control, AOT current mode control, hysteresis current mode control …etc. The experiment

TABLE V
COMPARISON OF THE PROPOSED PPRM CONTROL WITH AC COUPLE WITH STATE-OF-THE-ART PAPERS

Publications		This work experiment	[20] 2020 circuit syst	[9] 2018 JSSC	[8] 2021 IEEE access	This work simulation	[26] 2022 circuit syst	[6] 2022 TPE	[5] 2021 JSSC
Control method		**PPRM with ac couple**	Ripple-based digital V^2	Ripple-based mixed-current AOT	Current mode hysteresis	**PPRM with ac couple**	PFFC	Current mode AOT	Current mode AOT with dual ramp
Technology		**Discrete**	DSP board	0.18-μm	0.18-μm	**SIMPLIS**	0.18-μm	0.18-μm	0.18-μm
Input voltage (V)		**3.3 – 4.2**	3.3	0.8 – 1.4	0.5 – 1	**3.3**	2.5 – 4.4	1.8 – 2.4	1.8 – 3.3
Output voltage (V)		**5**	5 – 10	1.8	1.8	**5**	5	3.3	3 – 4.5
Max. load current (mA)		**2600**	3000	400	100	**2500**	1000	600	700
L (μH) / R_{DCR} (mΩ)		**8.8/114**	21/NA	1/NA	1/NA	**0.47/ 43**	1/9	0.1/NA	0.3/NA
C_{out} (μF)		**40**	500	6.8	10	**8**	20	1.41	6.6
Switching frequency (f_s)		**200 kHz**	50 kHz	750–860 kHz	550 kHz	**2.4 MHz**	2 MHz	15 MHz	10 MHz
Power consumption of current sensor (W)		**PR circuit 9.4 m (SIMPLIS) Max: 28 m (14)**	NA	NA	**NA**	**PR circuit 4.8 μ (SIMPLIS) Max: 13.8 μ (14)**	NA	Load: 500 mA 350 μ	Load: 300 mA 806 μ Load: 10 mA 83 μ
Peak efficiency		**92.5%**	NA	92.4%	88.5%	**92.6%**	95.2%	91.5%	94.5%
Load transient	I_{step} (mA)	500 – 1500	1000 – 3000	10 – 400	10 – 100	**0 – 1000**	10 – 1000	100 – 500	10 – 500
	Up	75 μs/ 320.7 mV(6.4%)	160 μs/ 380 mV(7.6%)	14 μs/ 126 mV(1.1%)	2 μs/ 20 mV(1.1%)	**4 μs/ 84 mV(1.6%)**	12 μs/ 41 mV(0.8%)	1 μs/ 105 mV(3.1%)	4 μs/ 125 mV(3.6%)
	Down	80 μs/ 298.4 mV(5.9%)	120 μs/ 160 mV(3.2%)	46 μs/ 150 mV(1.2%)	2 μs/ 22 mV(1.2%)	**5μs/ 76 mV(1.5%)**	26 μs/ 56 mV(1.1%)	1 μs/ 115 mV(3.4%)	27 μs/ 135 mV(3.9%)
FOM_{shoot} (Up/Down)		**0.559 /0.521**	1.5/0.6	5.5/6.5	22.2/24.4	**0.57/0.51**	0.82/1.13	6.1/6.7	8.0/8.6

The bold parts experiment result and simulation result of author's proposed circuit.

result of this work has 200 kHz switching frequency, and it is compared with [8], [9], [20] whose switching frequency is also below 1 MHz. The simulation result of this work has 2.4 MHz switching frequency, and it is compared with [5], [6], [26] whose switching frequency is above 1 MHz. Our experiment result has best FOM_{shoot} compared with [8], [9], [20]. Our simulation result also has best FOM_{shoot} compared with [5], [6], [26].

VI. CONCLUSION

A boost converter with PPRM control and ac couple is proposed to achieve a fast load-transient response. The proposed PR avoids the negative effect of the inductor current slope to load transient response. The proposed ac couple concept, which is well explained by the proposed small-signal model, further reduces the quality factor of the complex pole in control to output transfer function. Thus, easier loop gain design and reduced ringing during load-transient are achieved. A boost converter with the proposed control is implemented for verification. The proposed small signal model matches well with both SIMPLIS simulation and experiment results. Compare PPRM control with ac couple to PCM control, the output voltage undershoot/overshoot during load step-up/down reduces to only 42% and 38%, respectively. The experiment and simulation results verified the superior load-transient response of the proposed control with the best figure-of-merit among the recent papers.

ACKNOWLEDGMENT

The authors would like to thank SIMPLIS Technologies Corporation, USA, for providing SIMPLIS simulation tool.

REFERENCES

[1] C. C. Lun, A. B. Marzuki, and S. H. Wei, "Analog front-end design implementation of USB2.0 OTG attach detection protocol," in *Proc. 4th Int. Conf. Intell. Adv. Syst.*, 2012, pp. 774–779.
[2] "Power management components for lithium-ion battery powered application," Richtek Cooperation, Taiwan, 2015.
[3] A. E. Aroudi, R. Haroun, M. Al-Numay, J. Calvente, and R. Giral, "A large-signal model for a peak current mode controlled boost converter with constant power loads," *IEEE J. Emerg. Sel. Topics Power Electron.*, vol. 9, no. 1, pp. 559–568, Feb. 2021.
[4] "AN-1994 modeling and design of current mode control boost converters," Texas Instruments, Application Report, Jan. 2010.
[5] W. Hong and M. Lee, "A 10-MHz current-mode AOT boost converter with dual-ramp modulation scheme and translinear loop-based current sensor for WiFi IoT applications," *IEEE J. Solid-State Circuits*, vol. 56, no. 8, pp. 2388–2401, Aug. 2021.
[6] W. Hong and M. Lee, "A 15–25-MHz and 1-μs/0.4-A load response AOT boost converter using an accurate feedforward-path current sensor," *IEEE Trans. Power Electron.*, vol. 37, no. 2, pp. 1205–1209, Feb. 2022.
[7] J.-J. Chen, Y.-S. Hwang, J.-A. Chen, C.-H. Lai, and Y. Ku, "A new ultra-fast-response low-transient-voltage boost converter suitable for low-voltage solar cells in wireless sensor networks," *IEEE Sensors J.*, vol. 22, no. 18, pp. 18202–18209, Sep. 2022.
[8] Y.-S. Hwang, J.-J. Chen, J.-X. Xu, H.-S. Yang, C.-H. Lai, and Y. Ku, "An improved fast-transient-response low-transient-voltage boost converter with pseudo-current hysteresis-controlled techniques," *IEEE Access*, vol. 9, pp. 127270–127277, 2021.
[9] C.-H. Huang, H.-H. Wu, and C.-L. Wei, "Compensator-free mixed-ripple adaptive on-time controlled boost converter," *IEEE J. Solid-State Circuits*, vol. 53, no. 2, pp. 596–604, Feb. 2018.
[10] Y.-P. Su, Y.-K. Luo, Y.-C. Chen, and K.-H. Chen, "Current-mode synthetic control technique for high-efficiency DC–DC boost converters over a wide load range," *IEEE Trans. Very Large Scale Integration Syst.*, vol. 22, no. 8, pp. 1666–1678, Aug. 2014.
[11] X. Jing and P. K. T. Mok, "A fast fixed-frequency adaptive-on-time boost converter with light load efficiency enhancement and predictable noise spectrum," *IEEE J. Solid-State Circuits*, vol. 48, no. 10, pp. 2442–2456, Oct. 2013.
[12] J.-C. Tsai, C.-L. Chen, Y.-H. Lee, H.-Y. Yang, M.-S. Hsu, and K.-H. Chen, "Modified hysteretic current control (MHCC) for improving transient response of boost converter," *IEEE Trans. Circuits Syst. I: Regular Papers*, vol. 58, no. 8, pp. 1967–1979, Aug. 2011.

[13] Y.-S. Hwang, J.-J. Chen, R.-L. Shih, and Y.-T. Ku, "A 2-μs fast-response step-up converter with efficiency-enhancement techniques suitable for cluster-based wireless sensor networks," *IEEE Trans. Very Large Scale Integration Syst.*, vol. 26, no. 1, pp. 216–220, Jan. 2018.
[14] R. Redl and J. Sun, "Ripple-based control of switching regulators—An overview," *IEEE Trans. Power Electron.*, vol. 24, no. 12, pp. 2669–2680, Dec. 2009.
[15] W. W. Chen and J. S. Lai, "Improving the transient response of voltage-mode controller with the ripple-based circuit for an on-chip buck converter," in *Proc. IEEE Energy Convers. Congr. Expo.*, 2018, pp. 1388–1395.
[16] Y.-C. Lin, C.-J. Chen, D. Chen, and B. Wang, "A ripple-based constant on-time control with virtual inductor current and offset cancellation for DC power converters," *IEEE Trans. Power Electron.*, vol. 27, no. 10, pp. 4301–4310, Oct. 2012.
[17] Y. Yan, F. C. Lee, S. Tian, and P.-H. Liu, "Modeling and design optimization of capacitor current ramp compensated constant on-time V^2 control," *IEEE Trans. Power Electron.*, vol. 33, no. 8, pp. 7288–7296, Aug. 2018.
[18] J. A. J. Lu, C. J. Chen, C. Y. Hong, and C. J. Tsai, "A novel ripple-coupling constant on-time controlled buck converter IC with highly digital charge-pump based error amplifier," in *Proc. IEEE Appl. Power Electron. Conf. Expo.*, 2019, pp. 1766–1769.
[19] G. Zhou, S. Z. He, X. Chen, and H. Cui, "Can V^2 control be applied to boost converter?," *Electron. Lett.*, vol. 50, no. 8, pp. 627–629, Apr. 2014.
[20] G. Zhou, G. Mao, S. Zhou, Z. Li, and M. Leng, "Digital valley V^2 control for boost converter with fast load-transient performance," *IEEE Trans. Circuits Syst. II: Express Briefs*, vol. 67, no. 10, pp. 2089–2093, Oct. 2020.
[21] T. Qian, "Subharmonic analysis for buck converters with constant on-time control and ramp compensation," *IEEE Trans. Ind. Electron.*, vol. 60, no. 5, pp. 1780–1786, May 2013.
[22] T. Qian, W. Wu, and W. Zhu, "Effect of combined output capacitors for stability of buck converters with constant on-time control," *IEEE Trans. Ind. Electron.*, vol. 60, no. 12, pp. 5585–5592, Dec. 2013.
[23] S. Jian, "Characterization and performance comparison of ripple-based control methods for voltage regulator modules," in *Proc. IEEE 35th Annu. Power Electron. Specialists Conf.*, 2004, vol. 5, pp. 3713–3720.
[24] D. Yun, H. Kim, D. Baek, S. Cho, J. Yoon, and J. Lee, "A fixed-frequency synchronous boost converter based on adaptive on-time control with a new reverse phase ripple injection compensation," in *Proc. IEEE Energy Convers. Congr. Expo.*, 2020, pp. 2244–2250.
[25] Y. Yan, P. H. Liu, F. Lee, Q. Li, and S. Tian, "V^2 control with capacitor current ramp compensation using lossless capacitor current sensing," in *Proc. IEEE Energy Convers. Congr. Expo.*, 2013, pp. 117–124.
[26] S. Alevoor et al., "A 95.2% efficiency DC–DC boost converter using peak current fast feedback control (PFFC) for improved load transient response," *IEEE Trans. Circuits Syst. I: Regular Papers*, vol. 70, no. 3, pp. 1097–1109, Mar. 2023.
[27] R. B. Ridley, "A new, continuous-time model for current-mode control (power convertors)," *IEEE Trans. Power Electron.*, vol. 6, no. 2, pp. 271–280, Apr. 1991.
[28] V. Vorperian, "Simplified analysis of PWM converters using model of PWM switch. Continuous conduction mode," *IEEE Trans. Aerosp. Electron. Syst.*, vol. 26, no. 3, pp. 490–496, May 1990.
[29] G. W. Wester and R. D. Middlebrook, "Low-frequency characterization of switched DC–DC converters," *IEEE Trans. Aerosp. Electron. Syst.*, vol. AES-9, no. 3, pp. 376–385, May 1973.
[30] S. Tian, F. C. Lee, P. Mattavelli, K.-Y. Cheng, and Y. Yan, "Small-signal analysis and optimal design of external ramp for constant on-time V^2 control with multilayer ceramic caps," *IEEE Trans. Power Electron.*, vol. 29, no. 8, pp. 4450–4460, Aug. 2014.
[31] I. C. Wei, C. Dan, L. Yu-Cheng, and C. Ching-Jan, "The stability modeling of ripple-based constant on-time control schemes used in the converters operating in DCM," in *Proc. Int. Conf. Renewable Energy Res. Appl.*, 2012, pp. 1–8.
[32] J. Li and F. C. Lee, "Modeling of V^2 current-mode control," *IEEE Trans. Circuits Syst. I: Regular Papers*, vol. 57, no. 9, pp. 2552–2563, Sep. 2010.
[33] W.-C. Liu, C.-J. Chen, C.-H. Cheng, and H.-J. Chen, "A novel accurate adaptive constant on-time buck converter for a wide-range operation," *IEEE Trans. Power Electron.*, vol. 35, no. 4, pp. 3729–3739, Apr. 2020.
[34] L. Kong, D. Chen, S.-F. Hsiao, C.-F. Nien, C.-J. Chen, and K.-F. Li, "A novel adaptive-ramp ripple-based constant on-time buck converter for stability and transient optimization in wide operation range," *IEEE J. Emerg. Sel. Topics Power Electron.*, vol. 6, no. 3, pp. 1314–1324, Sep. 2018.
[35] "Demystifying the operational transconductance amplifier," Texas Instruments, Application Report, May 2009.

Yi-Rong Huang received the B.S. degree in electrical engineering from the Department of Electrical Engineering, National Chiao Tung University, Hsinchu, Taiwan, in 2015, and the M.S. degree in power electronic from the Graduate Institute of Electrical Engineering, National Taiwan University, Taipei, Taiwan, in 2017.

From 2017 to 2018, he was an Electric Engineer with Garmin Corporation, Taoyuan, Taiwan. From 2019 to 2020, he was an Engineer with IC Research and Development Department, Richtek Technology Corporation, Hsinchu, Taiwan.

Ching-Jan Chen (Senior Member, IEEE) received the B.S. and Ph.D. degrees in electrical engineering from National Taiwan University, Taipei, Taiwan, in 2006 and 2011, respectively.

From 2010 to 2011, he was a Visiting Scholar with the Center of Power Electronic Systems (CPES), Virginia Tech., Blacksburg. From 2011 to 2015, he was a Senior IC Research and Development Engineer with Richtek Technology Corporation, Hsinchu, Taiwan, which is Asia's No. 1 fabless power IC company and CPU power IC supplier according to revenue. His work was focused on new control scheme development and IC design of the voltage regulator controller for CPU power. In 2015, he became an Assistant Professor at the Department of Electrical Engineering, National Taiwan University, where he is currently an Associate Professor. His current research interests include control, modeling, and power IC design of dc–dc and ac–dc power converters for CPU and mobile devices, and GaN driver IC design.

Dr. Chen was the recipient of the Young Researcher Award from the Electrical Power Engineering Division, Ministry of Science and Technology (MOST), Taiwan, in 2016, the Outstanding Teaching Award from NTU in 2020, the Research Contribution Award from NTU EECS in 2020, and Ta-You Wu Memorial Award from MOST, Taiwan, in 2021. He was the corecipient of the 2019 IEEE Transportation Electrification Conference Asia-Pacific (ITEC-AP) Best Paper Award and the 2018 International Workshop on Power Supply on Chip (PwrSoC) Best Poster Award. He served more than 16 times as a Session Chair, Topic Chair, and Financial Chair in several IEEE conferences and competitions, such as ECCE, ECCE-Asia, International Future Energy Challenge (IFEC), IFEEC, WiPDA Asia, ITEC-Asia Pacific, and VLSI-DAT. He is the Secretary and then Vice-Chair of the IEEE PELS Taipei Chapter since 2018 and received the IEEE PELS Best Chapter Award in 2018. He is an Associate Editor for IEEE TRANSACTIONS ON POWER ELECTRONICS. He is a Senior Member of the IEEE Power Electronics Society.

Jia-Cheng Wu received the B.S. degree in electrical engineering from the Department of Electrical Engineering, National Central University, Taoyuan, Taiwan, in 2017, and the M.S. degree from the Graduate Institute of Electrical Engineering, National Taiwan University, Taipei, Taiwan, in 2022.

Tsung-Wei Huang received the M.S. degree in mechanics engineering from the Institute of Applied Mechanics, National Taiwan University, Taipei, Taiwan, in 2000.

He joined Richtek Technology, Ltd., Hsinchu, Taiwan, where he is currently a Senior Manager of mobile business unit.